



This document is a postprint version of an article published in *Expert Systems with Applications*© Elsevier after peer review. To access the final edited and published work see <https://doi.org/10.1016/j.eswa.2022.117765>

Document downloaded from:



12 Automatic marbling prediction of sliced dry-cured ham  
13 using image segmentation, texture analysis and  
14 regression

15 Eva Cernadas<sup>a</sup>, Manuel Fernández-Delgado<sup>a</sup>, Elena Fulladosa<sup>b</sup>, Israel  
16 Muñoz<sup>b</sup>

*<sup>a</sup>Centro Singular de Investigación en Tecnoloxías Intelixentes da USC (CiTIUS),  
Universidade de Santiago de Compostela, Rúa Xenaro de la Fuente Domínguez, Santiago  
de Compostela, 15782, Spain*

*<sup>b</sup>IRTA-TA, Food processing and Engineering, Finca Camps i Armet,  
Monells, Girona, 17121, Spain*

---

17 **Abstract**

Dry-cured ham is a traditional Mediterranean meat product consumed throughout the world. This product is very variable in terms of composition and quality. Consumer's acceptability of this product is influenced by different factors, in particular, visual intramuscular fat and its distribution across the slice, also known as marbling. On-line marbling assessment is of great interest for the industry for classification purposes. However, until now this assessment has been traditionally carried out by panels of experts and this methodology cannot be implement in industry. We propose a complete automatic system to predict marbling degree of dry-cured ham slices, which combines: 1) the color texture features of regions of interest (ROIs) extracted automatically for each muscle; and 2) machine learning models to predict the marbling. For the ROIs extraction algorithm more than the 90% of pixels of the ROI fall into the true muscle. The proposed system achieves a correlation

of 0.92 using the support vector regression and a set of color texture features including statistics of each channel of RGB color image and Haralick's coefficients of its grey-level version. The mean absolute error was 0.46, which is lower than the standard deviation (0.5) of the marbling scores evaluated by experts. This high accuracy in the marbling prediction for sliced dry-cured ham would allow to deploy its application in the dry-cured ham industry.

18 *Keywords:* Dry-cured ham, intramuscular fat, marbling, support vector  
19 regression, texture analysis, image segmentation

---

## 20 **1. Introduction**

21 Dry-cured ham is a traditional meat product of many Mediterranean  
22 countries that is widely consumed throughout the world, being its flavour  
23 and texture characteristics highly appreciated by consumers. There are many  
24 factors affecting the final characteristics of dry-cured ham, such as processing  
25 conditions and raw material characteristics, i.e. fat content (Coll-Brasas et al.,  
26 2021). In sliced dry-cured ham, visual intramuscular fat, subcutaneous fat  
27 thickness and color are the parameters most used by the consumers for the  
28 product evaluation, therefore affecting consumer's acceptability and purchase  
29 decision (Lorido et al., 2019). Although several non-invasive technologies  
30 can be used to categorize entire hams according to its fat content  
31 (de Prados et al., 2015), these technologies cannot be used to predict intramuscular  
32 fat (IMF) in sliced products because of its variability between the  
33 muscles of a ham.

34 Eating quality in meat has been associated to the fat distribution rather  
35 than to the total IMF. Distribution of IMF is usually known as marbling,  
36 because of its appearance similar to marble (Cernadas et al., 2002). One  
37 of the most important challenges for producers is the heterogeneity of the  
38 marbling in slices, that can vary significantly among ham pieces and even  
39 within the same piece. Classification of slices of dry-cured ham according to  
40 the marbling degree is of special interest for the food industry. Producers  
41 would be able to segment the market, offering products tailored to consumer's  
42 needs and increasing the value of their production.

43 Marbling ranking in different meats and meat products has been per-  
44 formed by panels of trained experts or relying on standards consisting of  
45 pictures depicting a scale of marbling (from 0.0 to 10.0), as it is the case  
46 for the National Pork Producers standards (Moines, 1999). In the case of  
47 dry-cured ham, a marbling ranking has been developed but it is not still  
48 published. However, marbling evaluations by experts are costly and are not  
49 feasible for the ham industry. Computer image analysis might be a solution  
50 because it is a fast and non-destructive technology, and it is a replicable and  
51 repetitive method that has been successfully applied to the assessment of  
52 multiple food characteristics: fish (Dutta et al., 2016), cheese (Dias et al.,  
53 2021) or bread (Srivastava et al., 2015). The scientific literature includes  
54 several studies that apply computer image analysis to determine IMF and  
55 marbling in different meat products. Combining magnetic resonance imag-  
56 ing (MRI) and computer vision techniques, the works (Cernadas et al., 2005;

57 *Ávila et al., 2019*) predicted marbling in the biceps muscle of dry-cured hams  
58 and loins, but MRI is a technology that is expensive to install in meat in-  
59 dustries.

60 For the segmentation of IMF in meat and meat products, several tech-  
61 niques have been applied: K-means clustering in beef *Longissimus dorsi*  
62 muscle (*Jackman et al., 2009*), automatic thresholding (*Liu et al., 2018*) and  
63 the Otsu method (*Uttaro et al., 2021*) in pork loin, multi-scale line detec-  
64 tion (*Cernadas et al., 2002*), gradient-based techniques (*Santos-Garcés et al.,*  
65 *2014*) and convolutional neural networks (*Muñoz et al., 2019*) for dry cured  
66 ham. In general, these segmentation algorithms perform quite well, high  
67 correlation values or low classification errors are obtained, depending on  
68 the aim of the study. For classification of marbling, the following tech-  
69 niques have been applied: chemical pre-treatments and line detection al-  
70 gorithms (*Faucitano et al., 2004*), line detection algorithm (*Liu et al., 2012*)  
71 and (*Huang et al., 2013*) in pork meat, neural networks (*Muñoz et al., 2015*)  
72 and decision trees in hyperspectral images of dry cured ham (*Velásquez et al.,*  
73 *2017*). In general, the results of marbling classification are quite satisfactory  
74 with low prediction errors and at least 90% of the samples correctly classified.  
75 However, the evaluation of IMF and marbling in dry-cured ham slices is still  
76 a challenge. A wide range of variation in the color of lean and fat tissues  
77 can be observed in slices across hams, which poses a challenge for image seg-  
78 mentation and the evaluation of marbling. These differences are explained  
79 by the different levels of drying of the hams, and the presence of precipitates

80 such as phosphates of tyrosine crystals, with a white color similar to that of  
81 the fat.

82 This paper proposes a prototype to automatically predict marbling of  
83 the principal muscles from a ham slice using image segmentation, texture  
84 analysis and regression models. Specifically, we define an algorithm that au-  
85 tomatically extracts squared regions inside the main muscles. Then, color  
86 texture features are computed for each region, which are the inputs to a re-  
87 gression model that predicts the marbling score for each muscle. The paper  
88 is organised as follows. Section 2 describes the materials used to obtain the  
89 ham slice, to develop the sensorial analysis on the ham muscles and to an-  
90 notate the contour of ham muscles. Section 3 describes the algorithm used  
91 to extract automatically the square ROIs representing each ham muscle, and  
92 briefly explains the color texture features extraction techniques and the re-  
93 gression models. Section 4 describes the experimental setup and statistical  
94 evaluation measures used. Section 5 presents and discusses the results. Fi-  
95 nally, section 6 summarises the main conclusions and proposals of future  
96 work.

## 97 **2. Materials**

98 This section describes the material used to obtain the data in this re-  
99 search: the system used to capture images of ham slice (subsection 2.1), the  
100 traditional procedures to determine the marbling of a ham muscle (subsec-  
101 tion 2.2), and the process to draw the outline of each muscle on the ham slice

102 (subsection 2.3).

### 103 *2.1. Image acquisition*

104 High quality images were acquired with a calibrated digital camera Canon  
105 EOS 50D (15.1 megapixels) and an objective Canon EF-S 18–200 mm f/3,5–  
106 5,6 IS. The camera was mounted in a black closet ( $1.06 \times 1.06 \times 2.50 \text{ m}^3$ ) with  
107 8 equidistant halogen lights Solux Q50MR16 CG/47/36°12 V/50 W/4700 K  
108 (Eiko Ltd., Shawnee, Kansas, U.S.A.) to ensure a correct lighting. White  
109 balance was carried out with a white card (Lastolite). The camera was  
110 connected to a computer to store the images. Slices were placed 30 cm below  
111 the camera on a uniform black surface. Photos of both sides of the dry-  
112 cured ham slices were taken. All the images were taken during the same  
113 session. The white balance of the images was carried out with Capture One  
114 PRO 5.0 software (Phase One A/S Inc., Frederiksberg, Denmark) and RGB  
115 images of  $667 \times 1000$  pixels with 16 bits color were obtained, with one pixel  
116 corresponding to  $0.3968 \text{ mm}^2$ . For the evaluation of marbling, the computer  
117 screen was calibrated so that the colors of the images were as close as possible  
118 to the colors of the samples (NEC Multisync LCD 2690 WUXI2). Figure 1  
119 shows a scheme of the image acquisition system used.

### 120 *2.2. Marbling evaluation*

121 Sensory analysis (marbling evaluation) of the samples was carried out by  
122 six trained panelists (ISO 8586-2: 2012) and consisted of a visual assess-  
123 ment of the marbling of the most representative muscles: *Biceps femoris*

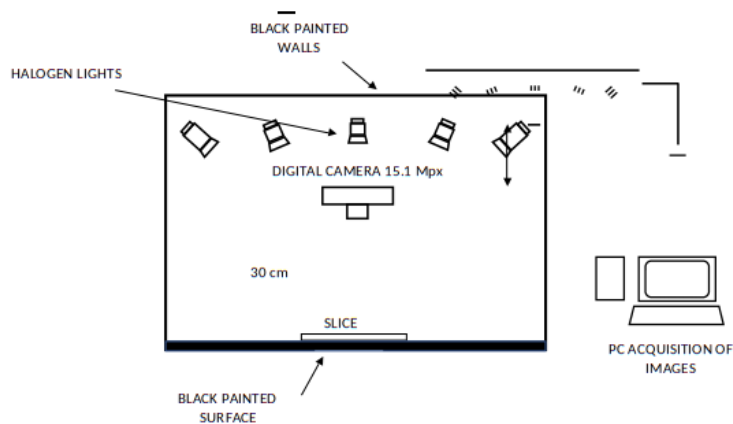


Figure 1: Scheme of the image acquisition system.

124 (BF), *Semimembranosus* (SM) and *Semitendinosus* (ST) of a dry-cured ham  
 125 (Bermúdez et al., 2014). Marbling was scored by consensus (in our case  
 126 three panelists) by means of scoring scale from 0.5 (minimum marbling) to  
 127 10 (maximum marbling) at intervals of 0.5. When scoring marbling, the  
 128 panelists considered the total amount and the distribution of the fat streaks.  
 129 Marbling evaluation was done in triplicate by the panelists. The standard  
 130 deviation of the panelists among trials was determined at 0.5 points.

Muscle	#images	Min.	Max.	Avg.	Dev.
Biceps femoris	337	1	7	3.1	1.0
Semimembranosus	322	0.5	6	2.0	1.0
Semitendinosus	55	4	9	6.2	1.2

Table 1: Number of images, minimum, maximum, average and standard deviation of the marbling values for the different ham muscles used in this experimentation.

131 A collection of commercial dry-cured hams were obtained from different  
 132 ham producers with crosses from different pig breeds (Large White, Lan-



133 drace, Duroc and Iberian) and having a wide range of marbling. A 2 cm  
134 thick slice containing muscles BF, SM and ST was obtained at 10 cm from  
135 the aitch bone in the distal direction (at the widest part of the ham) and  
136 packed into plastic bags of polyamide/polyethylene (oxygen permeability of  
137  $50 \text{ cm}^3/\text{m}^2/24 \text{ h}$  at  $23^\circ\text{C}$  and water permeability of  $2.6 \text{ g}/\text{m}^2/24 \text{ h}$  at  $23^\circ\text{C}$   
138 and 85% RH, Sacoliva<sup>©</sup> S.L., Spain). The image dataset is composed of  
139 714 images obtained in the following way: photos were obtained from 180  
140 commercial dry-cured hams, 2 slices/ham (at different points in the ham, ob-  
141 taining slices quite different one from another) and 2 muscles for each slice,  
142 giving a total of  $180 \text{ hams} \times 2 \text{ slices} \times 2 \text{ muscles} = 720$  photos. Six of these  
143 photos were not included in the evaluation due to defects on the surface such  
144 as cuts and phosphate crystals. For each image, it was only provided the  
145 measure of marbling for one muscle with values between 0.5 and 9 with the  
146 distribution shown in table 1. Figure 2 shows examples of different marbling  
147 scores for biceps muscle.

### 148 *2.3. Muscle annotation*

149 To develop the first experiment, the experts delineated the contour of the  
150 muscle for which the marbling was estimated by sensorial analysis. To draw  
151 the contours for all images, they used a home-made software, as it can be  
152 seen in figure 3.

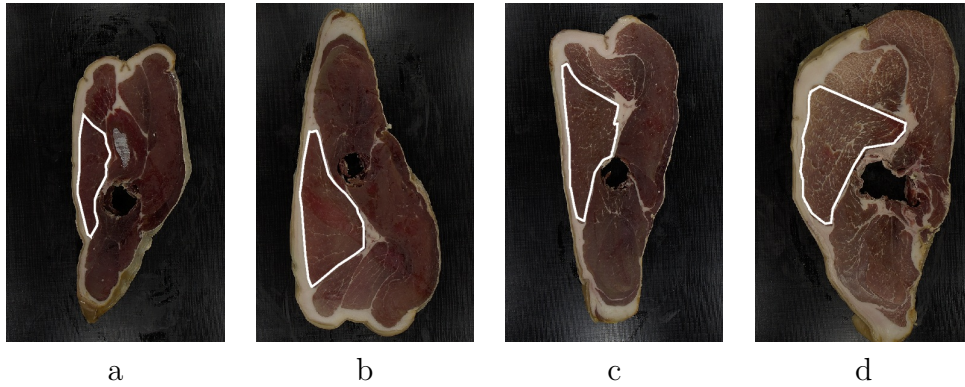


Figure 2: Examples of marbling scores for biceps muscle: a) slice 8372 with score 1; b) slice 8485 with score 1; c) slice 8274 with score 3; and d) slice 8424 with score 6.5.

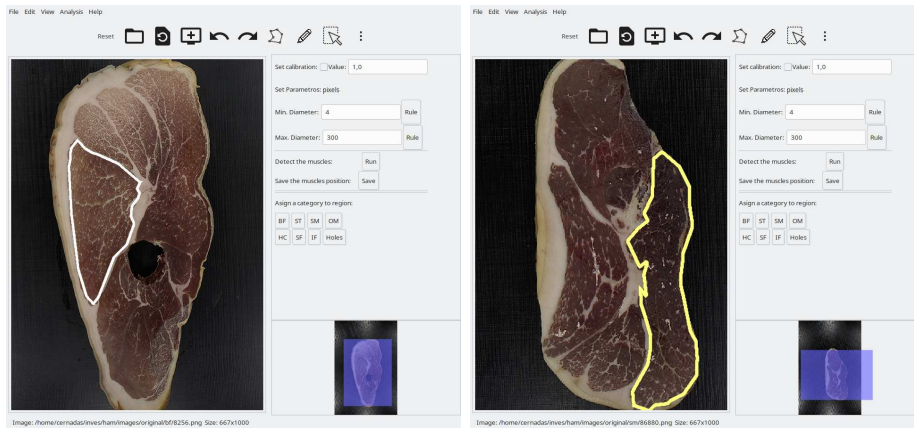


Figure 3: Examples of the contours of biceps (left panel) and semimembranosus (right panel) muscles overlapped to images of ham slice.

### 153 3. Methods

154 The system proposed to predict the marbling from dry-cured ham slices,  
 155 shown in figure 4, encloses the following stages: 1) the image acquisition  
 156 system already described in section 2.1; 2) the automatic extraction of the  
 157 ROIs in the ham slice; 3) the computation of features from the ROI extracted;

158 and 4) the regression model to predict the marbling score of each muscle in  
 159 the ham slice. The subsections 3.1, 3.2 and 3.3 describe the stages 2, 3 and  
 160 4, respectively.

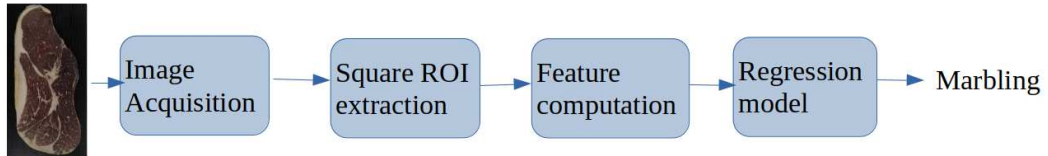


Figure 4: Stages of the method to predict the marbling from dry-cured ham slices.

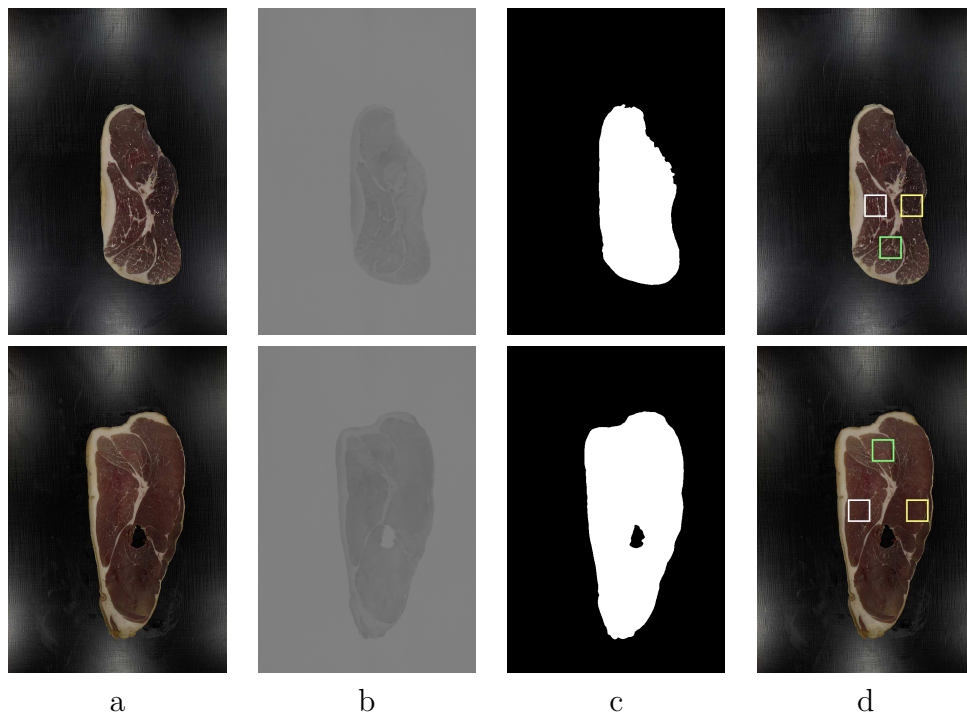


Figure 5: Examples of the extraction of square ROIs from the ham slice for all muscles: a) original images; b) channel *b* of Lab color space after smoothing; c) binary mask with the ham slice and bone hole and d) the extracted ROIs for each muscle, white for biceps, yellow for semimembranosus and green for semitendinosus.

161 *3.1. Automatic extraction of ROIs*

162 The ham slice images are processed to automatically extract square ROIs  
163 from the biceps femoris, semimembranosus and semitendinosus muscles. These  
164 extracted ROIs will be used in the third experiment. In this process, we take  
165 into account the anatomical information about the distribution of the mus-  
166 cles and subcutaneal/intermuscular fat within the ham. As it can be seen in  
167 figure 3, some slices present a hole in the slice (left panel), due to the slice  
168 is cut by the ham bone, and others not (right panel). As well, the biceps  
169 muscle can be in the right or left side of the image. The algorithm to extract  
170 the square ROIs encloses the following steps: 1) extract the ham slice from  
171 the image; 2) check if the slice has the bone hole; 3) if there is not a hole  
172 in the slice, find the biggest intermuscular fat region in the slice; 4) in both  
173 previous cases (step 2 or 3), a reference position is calculated to know the  
174 slice orientation, which allows to know if the muscles are upper/bottom or if  
175 the BF muscle is on left/right side of the slice; and 5) extract a square region  
176 for each muscle. In our case, we use a ROI with length  $s = 64$  pixels.

177 To extract the ham slice, the original RGB image  $I(x, y)$ , with  $x =$   
178  $1, \dots, N$ , and  $y = 1, \dots, M$ , of dimensions  $N \times M$ , is transformed to the  
179 Lab color space, because it is more robust to illuminance variance than the  
180 RGB space (Cernadas et al., 2017). Let  $I_b(x, y)$  be the  $b$  channel of the ham  
181 slice after smoothing with a mask (we use a mask of 5 pixels) in order to  
182 attenuate the small fat features and noise ( column b in figure 5). Let  $h_b$  be  
183 the histogram of image  $I_b(x, y)$ . The maximum value  $H_b$  of  $h_b$  is chosen to

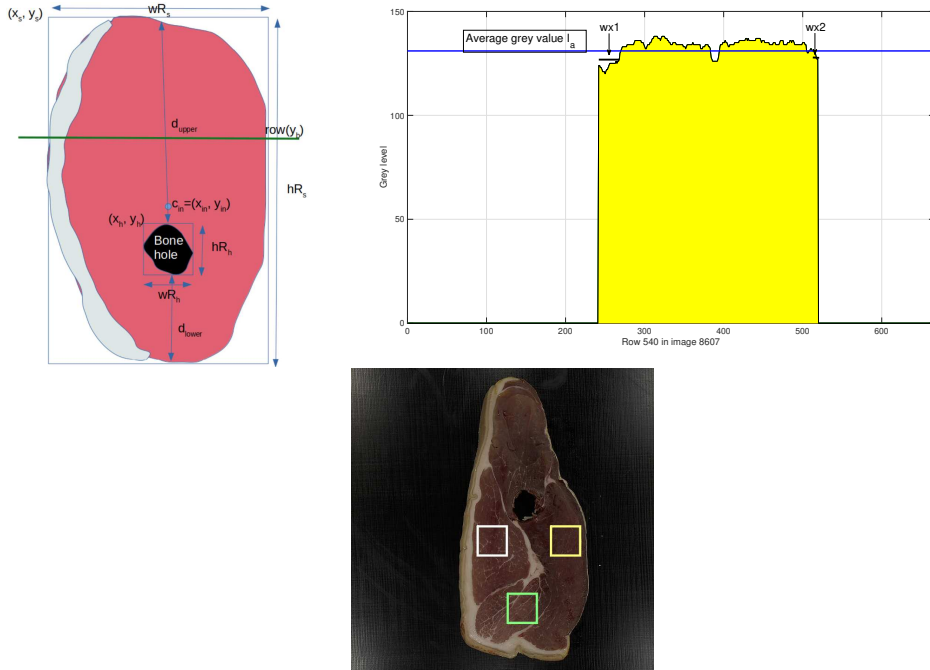


Figure 6: Extraction of the square ROIs of each muscle. Upper left panel: scheme of a ham slice. Upper right panel: row 540 of the transformed version  $I_a$  of the ham slice no. 8607. Lower panel: the ham slice with the extracted ROIs overlapped: *biceps* (white), *semimembranosus* (yellow) and *semitendinosus* (green).

184 calculate the area of ham slice. The  $I_b(x, y)$  image is thresholded to calculate  
 185 the binary image  $B(x, y)$  using the following expression:

$$B(x, y) = \begin{cases} 0 & |I_b(x, y) - H_b| \leq 5 \\ 255 & \text{otherwise} \end{cases} \quad (1)$$

186 After thresholding, we apply morphological operators to the binary image  
 187  $B$  in order to fill small holes. First, the biggest region of  $B$  is extracted and it

---

**Algorithm 1:** Automatic extraction of square ROI images for each muscle from a ham slice.

---

1 **Algorithm:**  $[I_{BF}, I_{SM}, I_{ST}] = \text{ExtractSquaredROI}(I, s)$

**Data:**  $I$ : original RGB image of ham slice;  $s$ : size of ROI  
**Result:**  $I_{BF}, I_{SM}, I_{ST}$ : square ROI images for *biceps*, *semimembranosus* and *semitendinosus* muscles

2  $I_b \leftarrow b$  channel of Lab image smoothed by box filter  
3  $h_b \leftarrow$  histogram of  $I_b$   
4  $H_b \leftarrow$  maximum of  $h_b$   
5  $B \leftarrow$  binary image using eq. 1 and morphological processing  
6  $B_m \leftarrow$  image mask with ham slice outline and hole if exist  
7  $R_s \leftarrow (x_s, y_s, wR_s, hR_s)$  rectangle enclosing ham slice  
8  $I_a \leftarrow a$  channel of Lab image smoothed and masked by  $B_m$   
9  $\mu_a \leftarrow$  average value of  $I_a$  inside  $B_m$ ; **offset** $\leftarrow 10$

10 **if existsHole**( $I_b$ ) **then**  
11      $R_h \leftarrow (x_h, y_h, wR_h, hR_h)$  rectangle enclosing hole  
12      $d_{upper} \leftarrow y_s - y_h$ ;  $d_{lower} \leftarrow y_s + hR_s - (y_h + hR_h)$   
13     **if**  $d_{upper} > d_{lower}$  **then**  
14          $y_c \leftarrow y_s - (y_s - y_h)/4$   
15          $y_e \leftarrow y_h - s/2 - \text{offset}$   
16     **else**  
17          $y_c \leftarrow y_s + hR_s - s - (y_s + hR_s - y_h - hR_h)/4$   
18          $y_e \leftarrow y_h + hR_h + s/2 + \text{offset}$   
19     **end**  
20      $x_c \leftarrow \text{middlePointX}(\text{row}(y_c + s/2))$   
21      $I_{ST} \leftarrow \text{extST}(x_c - s/2, y_c, s)$   
22      $[I_{BF}, I_{SM}] \leftarrow \text{extBSM}(y_e)$

23 **else**  
24      $T_2 \leftarrow$  second Otsu's threshold of  $I_a$   
25      $(x_{in}, y_{in}) \leftarrow$  centroid of the largest inner region inside  $I_a$  after  
       thresholding using  $T_2$   
26      $I_{ST} \leftarrow \text{extSTC}(x_{in}, y_{in}, s)$   
27      $[I_{BF}, I_{SM}] \leftarrow \text{extBSM}(y_{in})$

28 **end**

---

188 is associated with the contour of ham slice. Next, the algorithm searches for  
189 a large black region inside this contour. If this region is found, it is associated  
190 to the bone hole. The contours of ham slice and bone hole are used to create  
191 a binary mask image  $B_m(x, y)=0$  (black color in column c of figure 5) when  
192  $(x, y)$  is inside the contour and outside the bone, and  $B_m(x, y)=1$  (white  
193 color) when  $(x, y)$  is outside the contour or inside the bone. This process  
194 is shown in the columns a, b and c of the figure 5. The process to extract  
195 the ROI for each muscle, denoted as  $I_{BF}$ ,  $I_{SM}$  and  $I_{ST}$  for *biceps femoris*,  
196 *semimembranosus* and *semitendinosus*, respectively, is drawn in figure 6 and  
197 summarized by algorithm 1. Let  $R_s$  be the rectangle enclosing the ham slice,  
198 which is defined by the top left vertex  $(x_s, y_s)$  and by its width ( $wR_s$ ) and  
199 height ( $hR_s$ ). Let  $I_a$  be the  $a$  channel of Lab image of the ham slice masked  
200 (multiplied) by  $B_m$ . Two cases can be considered:

- 201 a) When the ham slice has visible bone hole, the algorithm uses as refe-  
202 rence its enclosing rectangle  $R_h$ , with initial coordinates  $(x_h, y_h)$  and  
203 width and height  $wR_h$  and  $hR_h$ , respectively.
- 204 b) When the ham slice has not a visible bone hole, the algorithm searches  
205 for the largest intermuscular fat region and calculates its centroid. In  
206 order to discard the background from the image  $I_a$ , we selected a thresh-  
207 old applying the Otsu's method (Otsu, 1979) with three thresholds  
208  $\{T_i\}_{i=1}^3$ , that correspond to different types of materials in the image  
209 (background, subcutaneous fat and muscle). Experimentally, we checked

210 that threshold  $T_2$  ensures an accurate segmentation of background from  
 211 the remaining materials. In the binary image generated by threshold-  
 212 ing  $I_a$  with  $T_2$ , the inner biggest region is selected as representing the  
 213 intermuscular fat region, whose centroid is  $(x_{in}, y_{in})$ .

214 These reference points (bone hole or centroid of intermuscular fat) allow  
 215 to select the height where the different muscles should be extracted. In order  
 216 to extract the BF and SM muscles, the algorithm finds out whether the biceps  
 217 is on the left or right side of the ham slice. The position in the horizontal  
 218 axis for extracting the BF and SM muscles is determined analysing a specific  
 219 row in the image  $I_a$ . This row is smoothed in order to attenuate the random  
 220 noise and it is denoted as  $\mathbf{row}(y_b) = I_a(x, y_b)$ ,  $x = 1, \dots, M$  (see upper left  
 221 panel of figure 6). In order to locate the BF muscle, we estimate the pixels  
 222 representing the subcutaneous fat (close to the *biceps* muscle) along the  $\mathbf{row}(y_b)$   
 223 counting the number of values. Specifically, the procedure is as follows:

- 224 1. Let  $k_1$  be the first value of  $x$  where  $I_a(x, y_b) > 0$  coming from left to  
 225 right (see the upper right panel of figure 6). Let  $wx1$  be the number of  
 226 values of  $x$  where  $I_a(x, y_b) < \mu_a$ , for  $x = k_1, k_1 + 1, \dots, M$  (i.e. going  
 227 from left to right side), where  $\mu_a$  is the average value of  $I_a$  inside  $B_m$ .
- 228 2. Let  $k_2$  be the first value of  $x$  where  $I_a(x, y_b) > 0$  coming from right  
 229 to left, and  $wx2$  the number of values that  $I_a(x, y_b) < \mu_a$ , for  $x =$   
 230  $k_2, k_2 - 1, \dots, 2, 1$  (i.e. going from right to left side).



231 If  $wx1 > wx2$  the BF muscle is on the left side of ham slice. Otherwise, it  
 232 is on the right side. This process is performed by the `extBSM(y)` function in  
 233 the algorithm 1, where  $y$  represents the row to be analysed in the image. So  
 234 the square ROIs for muscles BF and SM, of size  $s$ , are extracted at positions  
 235  $(k_1 + wx1 + s/2 + \text{offset}, y)$  and  $(k_2 - wx2 - s/2 - \text{offset}, y)$  (we use an offset of  
 236 10 pixels in order to avoid defects in the contour of ham slice). The regions  
 237 extracted for each muscle are shown overlapped to the ham slice in the column  
 238 d of the figure 5. When there is bone hole, the  $y$  coordinate for extracting  
 239 muscles are determined calculating the distances  $d_{upper} = y_s - y_h$  and  $d_{lower} =$   
 240  $y_s + hR_s - (y_h + hR_h)$ . If  $d_{upper} > d_{lower}$ , the muscles are above the bone  
 241 hole, otherwise the muscles are below the bone hole. The `middlePointX(y)`  
 242 function returns the middle point of the ham slice for the image row  $y$ . The  
 243 `extST(x, y, s)` function extracts a square ROI of size  $s$  for the ST muscle  
 244 from the original RGB image in the point  $(x, y)$  for ham slices with visible  
 245 hole. The `extSTC(x, y, s)` function extracts a square ROI of the ST muscle  
 246 for ham slices without visible hole. Let  $x_{c1} = \text{middlePointX}(\text{row}(y_{in} + s/2))$   
 247 and  $x_{c2} = \text{middlePointX}(\text{row}(y_{in} - s/2))$  be two middle points in the ham  
 248 slice in the horizontal axis near the centroid of intermuscular fat. Let  $r_1$   
 249 and  $r_2$  be two ROIs of size  $s$ , extracted from the image  $I_a$  in the points  
 250  $(x_{c1} - s/2, y_s - (y_s - y_{in})/6)$  and  $(x_{c2} - s/2, y_s + wR_s - s - (y_s + wR_s - y_{in})/3)$   
 251 respectively. To select which ROI corresponds to the ST muscle, the mean  
 252 value of both ROIs,  $\mu_{r1}$  and  $\mu_{r2}$ , are calculated and the ST muscle is the ROI  
 253 with the highest mean value, which corresponds with the ROI containing

254 more fat.

### 255 3.2. Color texture features

256 Texture analysis has been employed in previous works to predict different  
257 qualities or attributes of meat products from MRI images (Cernadas et al.,  
258 2005; Ávila et al., 2019), which are grey level images. Nevertheless, it is  
259 known that the color is also a very important characteristic in other computer  
260 vision applications (González-Rufino et al., 2013; Cernadas et al., 2017). Color  
261 texture analysis can be tackled from different paradigms: simple color fea-  
262 tures, grey level texture features and integrative color texture analysis. A  
263 recent work (Cernadas et al., 2017) concluded that parallel approaches, that  
264 concatenate the two former, are superior than analysing directly the color  
265 texture with integrative approaches.

266 There are many methods to extract only the color in a strict sense (Cernadas et al.,  
267 2017). In this work we use two color spaces, RGB and Lab, where the chro-  
268 matic channels are  $a$  and  $b$ . We use first-order features of three types, each  
269 with 2 feature vectors:

- 270 1. Only mean value for each chromatic channel, denoted as CM, that  
271 stands for “color mean”: 1) **CMRGB**, 3 features: mean color of the  
272 channels R, G, and B of the muscle; 2) **CMab**, 2 features: mean color  
273 of the channels  $a$  and  $b$  of the Lab image. In both cases, the mean  
274 values are only calculated inside the muscle regions.
- 275 2. Mean and variance for each chromatic channel, CMV, or color mean

276 and variance: 1) **CMVRGB**, 6 features: mean and variance of the  
277 channels R, G and B of the RGB image. 2) **CMVab**, 4 features: mean  
278 and variance of the channels  $a$  and  $b$  of the Lab image.

279 3. First order statistics, denoted as FOS, for each chromatic channel, that  
280 include mean, variance, skewness, kurtosis and entropy: 1) **FOSRGB**,  
281 15 features: 5 features  $\times$  3 color channels of the RGB image. 2)  
282 **FOSab**, 10 features: 5 features  $\times$  2 color channels of the Lab image.

283 The most popular grey level texture features belong to the families of  
284 statistical, such as second-order features and local binary patterns (LBP),  
285 and frequencial, including wavelet and Gabor features. The grey level version  
286 of the original image is obtained following two alternative approaches: 1)  
287 converting a RGB image to grey level image; and 2) using the L channel of  
288 a Lab image.

289 Among the second-order statistics we selected the Haralick coeficients  
290 (Haralick et al., 1973), derived from the grey level coocurrence matrix (GLCM).  
291 These coeficients describe the probability of finding two pixels with the same  
292 value at different scales, or distances, and orientations, or angles. The pa-  
293 rameters used normally are: 1) the orientations  $0^\circ$ ,  $45^\circ$ ,  $90^\circ$  and  $135^\circ$ ; and 2)  
294 three scales, with pixel distances of 1, 2, and 3. For each scale, the GLCM  
295 matrix is averaged over all orientations, and the contrast, homogeneity, cor-  
296 relation and energy of the matrix is computed. Two feature vectors were  
297 considered: 1) **HarRGB**, that includes the four previous features for scales

298 {1, 2, 3} calculated on the grey version of the RGB image, with  $4 \times 3 = 12$  fea-  
299 tures; and 2) **HarLab**, which is similar to **HarRGB** but calculated on the  
300 L channel of Lab image. When the input is an irregular region, the features  
301 are computed only on pixels included in the region (González-Rufino et al.,  
302 2013). The Haralick’s coefficients were computed using the `graycomatrix()`  
303 function of the Matlab Image Processing Toolbox<sup>1</sup>.

304 The LBP operator is a state-of-art texture analysis approach proposed by  
305 Ojala et al. (2002), which describes each pixel comparing its value with the  
306 neighboring pixels. For each neighboring pixel, the result will be set to one  
307 if its value is higher than the value of central pixel, otherwise the result will  
308 be set to zero, developing a binary code for each pixel. We use the uniform  
309 LBP, which considers the binary patterns with only two transitions (from  
310 0 to 1 and vice versa). In a circularly symmetric neighbor set of  $P$  pixels  
311 can occur  $P + 1$  uniform binary patterns. The number of “1’s” in the binary  
312 pattern is the label of the pattern, while the nonuniform patterns are labelled  
313 by  $P + 1$ . This process can be applied to different scales, as in the case of  
314 cooccurrence image. The histogram of the pattern labels accumulated over  
315 the intensity image is employed as texture feature vector. The most common  
316 values for these parameters are  $\{(P, R) \in (8, 1), (12, 2), (16, 3)\}$ , where  $P$  is  
317 the number of neighbors and  $R$  is the distance between the central pixel  
318 and the neighbors. We construct the texture feature vectors **LBPRGB** and

---

<sup>1</sup><https://www.mathworks.com>

319 **LBPLab** to be applied on the grey version on RGB image and on the L  
320 channel of the Lab image, respectively. Both vectors have  $42 = (8 + 2) +$   
321  $(12 + 2) + (16 + 2)$  features, because the uniform LBP are  $P + 2$  features. We  
322 use the LBPMatlab<sup>2</sup> implementation provided by the LBP creators.

323 Discrete wavelet transform (DWT) representation is a theory for multi-  
324 dimensional signal decomposition (Walker, 2008; Laine and Fan, 1993) which  
325 recursively apply filters to decompose the image into low-pass and high-  
326 pass frequency bands. A compact representation for texture analysis can  
327 be computed taking the mean and variance of the energy distribution for  
328 the transformed coefficients in each sub-band and decomposition level. We  
329 compute texture feature vectors calculating the mean and variance of the  
330 energy over 3 levels of decomposition and create the feature vectors  $\mathbf{WT}_{ijk}$ ,  
331 where: 1)  $i = \{Haar, Daub\}$  is the type of filters to use, namely Haar (2  
332 coefficients) or Daubechies filtering with four coefficients; 2)  $j = \{RGB, Lab\}$   
333 is the grey level version of the RGB image or the L channel of the Lab image;  
334 and 3)  $k = \{LL, All\}$  represents if only the low-low decomposition sub-bands  
335 are considered ( $6 = 2 \times 3$  features) or all the sub-bands ( $24 = 2 \times 3 \times 4$   
336 features). We used the functions `wfilters()` and `dwt2()` of the Matlab  
337 Wavelet Toolbox.

338 Gabor filters are sinusoidal waves modulated by a Gaussian envelope  
339 that can be used for texture classification (Randen and Husoy, 1999). The

---

<sup>2</sup><http://www.cse.oulu.fi/CMV/Downloads/LBPMatlab>

340 filters are applied to the images varying their frequency and orientation.  
341 Bianconi and Fernández (2007) analysed the influence of these parameters  
342 for texture classification. After applying a set of digital Gabor filters  $G_{ij}(x, y)$   
343 with  $i \in \{1, \dots, n_F\}$  and  $j \in \{1, \dots, n_O\}$ , where  $n_F$  and  $n_O$  are respectively  
344 the number of frequency and orientations, some statistical features are com-  
345 puted over each filtered image. We used the `gabor()` and `imgaborfilt()`  
346 functions of the Matlab Image Processing Toolbox considering the wave-  
347 lengths  $[3, 6, 9, 12]$  and orientations  $[0, 30, 60, 90, 120, 150]$ , recommended by  
348 (Bianconi and Fernández, 2007). We compute the feature vectors **Gabor-**  
349 **RGB** and **GaborLab**, both with 48 features, that include the mean and  
350 standard desviation for each filter ( $n_F \times n_O = 6 \times 4 = 24$  filters) applied on  
351 the grey level version of the RBG image or the L channel of the Lab image,  
352 respectively.

### 353 *3.3. Regression models*

354 We selected for this experimentation several state-of-art regression models  
355 of different families that provided good performances in the comparative  
356 analysis (Fernández-Delgado et al., 2019). One of them is implemented in  
357 the Octave<sup>3</sup> scientific programming language, and the remaining ones in the  
358 R<sup>4</sup> statistical computing language. Most regressors in our collection have  
359 tunable hyper-parameters, i.e., parameters whose values must be specified

---

<sup>3</sup><http://www.octave.org>

<sup>4</sup><http://www.r-project.org>

360 previously to training, that often have a strong influence on the regressor  
361 performance. In these cases, it is a good practice to try several values for each  
362 hyper-parameter in a trial-and-error procedure, and to select the value that  
363 provides the best performance on a separate data collection. This method is  
364 called “grid search” tuning. The following is a list of these regressors, with  
365 its tunable hyper-parameters and the list of values tried for each one in the  
366 grid search. For the regressors programmed in R, these values were provided  
367 by the `getModelInfo()` function of the `caret` R package (Kuhn, 2016).

- 368 1. **lm** is the linear regression provided by the `stats` R package, which per-  
369 forms multivariate linear regression and has no tunable hyper-parameter  
370 (Bates and Chambers, 1992).
- 371 2. **svr**: epsilon-support vector regression with radial basis function kernel,  
372 using the `LibSVM` library (Chang and Lin, 2011) through its Octave in-  
373 terface. The regularization hyper-parameter  $C$  and  $\gamma = 1/2\sigma^2$ , where  
374  $\sigma$  is the kernel spread, are tuned with values  $\{2^i\}_{-5}^{15}$  and  $\{2^i\}_{-10}^{10}$ , re-  
375 spectively.
- 376 3. **M5**: regression tree (Quinlan, 1992) implemented by the Weka Data  
377 Mining Software<sup>5</sup> and accessed from a R program through the `RWeka`  
378 package. It has no tunable hyper-parameter.
- 379 4. **cubist**: M5 rule-based regressor with corrections based on nearest

---

<sup>5</sup><http://www.cs.waikato.ac.nz/ml/weka>

380 neighbors in the training set (Quinlan, 1993), implemented by the  
381 `Cubist` R package. Its tunable hyper-parameters are the number of  
382 neighbors [0,5,9] and the number of committees [1,10,20].

383 5. **gbm**: generalized boosting regression model (`gbm` R package) with  
384 Gaussian distribution. The tunable hyper-parameters are the maxi-  
385 mum depth of input interactions, with values [1,2,3,4,5] and the number  
386 of trees for prediction, with values from 50 to 250 step 50.

387 6. **rf**: random forest (Breiman, 2001) ensemble of averaged random regres-  
388 sion trees (`randomForest` R package). The number of inputs selected  
389 at each tree (`mtry`) is tuned with 10 values between 2 and the number  
390 of features.

#### 391 4. Experimental setup

392 In order to achieve a fully automatic system, which can operate on-line  
393 in the meat industries, we will develop three experiments to compare the  
394 computer predictions with the sensorial procedures:

395 1. **Experiment 1**: prediction of the marbling from irregular regions of the  
396 ham muscles that are delineated and annotated by the food technology  
397 experts. In this case, the prediction is done using the same information  
398 (irregular region) as the experts.

399 2. **Experiment 2**: prediction of the marbling using square regions ex-  
400 tracted from the irregular regions of the experiment 1. This experiment



401 tests the reduction of performance when a region of the slice smaller  
402 than the whole irregular region is used to do the prediction.

403 **3. Experiment 3:** fully automatic extraction of square regions of interest  
404 (ROI) for each ham muscle, and prediction of the marbling using these  
405 ROIs. This experiment will test the performance loss when the ROI  
406 extraction may be suboptimal, but the method is fully automatic and  
407 does not require any food technology expert.

408 In order to test the performance of the ROI extraction algorithm, we  
409 define the overlapping percentage (OP) as:

$$OP_m = 100 \frac{NO_m}{R_t} \quad (2)$$

410 where  $m$  may be biceps, semimembranosus or semitendinosus,  $R_t$  is the num-  
411 ber of pixels of the ROI (in our case  $s^2=64 \times 64=4,096$  pixels) and  $NO_m$  is  
412 the number of pixels overlapped to the true region annotated by the expert  
413 for the muscle  $m$ .

414 To test the performance of regression models in the prediction of marbling,  
415 we used the classical K-fold cross-validation methodology, which uses training  
416 and test sets. The most popular performance measures are the Pearson's  
417 correlation coefficient ( $R$ ) between the true and predicted marbling, the mean  
418 absolute error (average absolute difference between the predicted and true  
419 marbling, MAE) and the root mean square error (square root of the mean

420 squared difference between them, RMSE):

$$R = \frac{\sum_{i=1}^N (y_i - \bar{y})(o_i - \bar{o})}{\sqrt{\left(\sum_{i=1}^N (y_i - \bar{y})^2\right) \left(\sum_{i=1}^N (o_i - \bar{o})^2\right)}} \quad (3)$$

$$MAE = \frac{1}{N} \sum_{i=1}^N |y_i - o_i| \quad (4)$$

$$RMSE = \sqrt{\frac{1}{N} \sum_{i=1}^N (y_i - o_i)^2} \quad (5)$$

421 where  $y_i$  and  $o_i$  are the predicted and true values of marbling respectively for  
422 ham slice  $i$ ,  $\bar{y}$  and  $\bar{o}$  are the mean values of  $\{y_i\}_{i=1}^N$  and  $\{o_i\}_{i=1}^N$ , respectively,  
423 and  $N$  is the number of ham slices. The  $|R|$  values can be interpreted ac-  
424 cording to Colton (1974) as: true and predicted values are not correlated at  
425 all (0-0.25), bad to moderate correlation (0.25-0.5), moderate to good (0.5-  
426 0.75), very good to excellent (0.75-1). In our study, we use  $K = 4$  folds or  
427 trials, devoting  $K - 2 = 2$  folds for training, one for validation and one for  
428 test. Since all the folds have the same size, 50%, 25% and 25% of the data  
429 are devoted to training, validation and test sets, respectively. In our case,  
430 each data corresponds to the image of a ham slice, and it is composed by the  
431 texture feature vector extracted from the image (input) and the marbling  
432 value (output) corresponding to that slice image. In order to guarantee that  
433 training, validation and test sets contain output values distributed across the

434 whole range of marbling values, the data are sorted by increasing marbling.  
435 After sorting, data 1, 2, 3 and 4 are included in folds 1, 2, 3 and 4, respec-  
436 tively. Data 5, 6, 7 and 8 are added to folds 1, 2, 3 and 4, respectively, and  
437 so on. Let  $\{T_k, V_k, S_k\}_{k=1}^K$  be the training, validation and test folds on  $k$ -th  
438 trial. Trial 1 uses folds 1 and 2 for training, fold 3 for validation and fold  
439 4 for test (see table 2). Trial 2 uses folds 2 and 3 for training, fold 4 for  
440 validation and fold 1 for test, and analogously for trials 3 and 4. Therefore,  
441 training, validation and test sets in all the trials include data with marbling  
442 values in the whole range of values, composing training sets of higher quality  
443 that are expected to allow regressors learn better.

$K=4$	Trial 1	Trial 2	Trial 3	Trial 4
Train	$T_1=\{1,2\}$	$T_1=\{2,3\}$	$T_1=\{3,4\}$	$T_1=\{4,1\}$
Validation	$V_1=\{3\}$	$V_1=\{4\}$	$V_1=\{1\}$	$V_1=\{2\}$
Test	$S_1=\{4\}$	$S_1=\{1\}$	$S_1=\{2\}$	$S_1=\{3\}$

Table 2: Distributions of folds in training, validation and test for each trial.

444 Table 2 reports the experimental methodology. For each combination  $C_i$   
445 of hyper-parameter values of the model, with  $i = 1, \dots, N$ , and for each trial  
446  $k$ , with  $k = 1, \dots, K$ , the set  $T_k$  is used to train the model using the com-  
447 bination  $C_i$  of hyper-parameter values, while the set  $V_k$  is used as validation  
448 set to evaluate the performance  $P_{ik}$  of the trained model using  $C_i$  on  $V_k$ .  
449 The average  $P_i$  of  $\{P_{ik}\}_{k=1}^K$  is thus the performance associated to the com-  
450 bination  $C_i$  of hyper-parameter values. The process is repeated for all the  
451 combinations  $\{C_i\}_{i=1}^N$ , and the combination  $C_I$  with the highest performance  
452  $I = \operatorname{argmax}\{P_i\}_{i=1}^N$  is selected. Then, for  $k = 1, \dots, K$  the model with this

453 best combination  $C_I$  is trained on the set  $\{T_k, V_k\}$ , that includes  $K - 1$  folds,  
 454 and tested on the set  $S_k$  (1 fold), achieving a performance  $P_k$ . The average  
 455 of  $\{P_k\}_{k=1}^K$  is the final test performance  $P$  of the model.

---

**Algorithm 2:** Experimental methodology, combining  $K$ -fold cross-validation and hyper-parameter tuning.

---

```

1 for  $i = 1 : N$  do
2   for  $k = 1 : K$  do
3     Train the model with  $C_i$  on dataset  $T_k$ 
4     Validate the model with  $C_i$  on dataset  $V_k$ 
5      $P_{ik}$ =performance with  $C_i$  on  $V_k$ 
6    $P_i$ =average of  $\{P_{ik}\}_{k=1}^K$ 
7  $I = \operatorname{argmax}\{P_i\}_{i=1}^N$ 
8 for  $k = 1 : K$  do
9   Train the model with  $C_I$  on  $\{T_k, V_k\}$ 
10  Test the model with  $C_I$  on  $S_k$ 
11   $P_k$ =performance with  $C_I$  on  $S_k$ 
12  $P$ =average of  $\{P_k\}_{k=1}^K$ 

```

---

## 456 5. Results and discussion

457 We present the results obtained from the different points of view: the au-  
 458 tomatic extraction of ROIs to represent each muscle (subsection 5.1), the per-  
 459 formance of marbling prediction model (subsection 5.2), comparison among  
 460 the performance of different prediction models (subsection 5.3), the method  
 461 stability with the muscles (subsection 5.4) and the computational time of the  
 462 different stages of the procedure (subsection 5.5).

463 *5.1. Extraction of ROIs*

464 We tested the performance of the automatic algorithm to extract square  
465 ROIs, of size  $64 \times 64$  pixels, for each muscle described in section 3.1, by  
466 using the measures described in eq. 2 of section 4 between the true muscle  
467 and the extracted ROI for each muscle  $m$ . We compared the results with  
468 the extraction done for experiment 2, in which the ROI is extracted from  
469 the centroid of the irregular region (muscle) annotated by the expert (see  
470 section 2.3). This extraction is normally satisfactory: in experiment 2, an  
471 overlapping of 100% is achieved for the 47% of images, and the overlapping  
472 is below 80% for only the 8% of the images. In experiment 3, the extraction  
473 is perfect for the 52% of images and the overlapping is lower than 80% for  
474 only the 12% of the images. Figure 7 shows some examples of suboptimal  
475 ROI extraction: for the ROI extraction using centroid (experiment 2), the  
476 causes of suboptimal extraction are muscles smaller than the ROI size (figure  
477 7a) and muscles not rounded (figure 7c). For the automatic ROI extraction  
478 (experiment 3), the causes of failure are: i) suboptimal extraction (figure 7d)  
479 and ii) exchange SM and ST muscles due to artefacts in the ham slice (figure  
480 7b). Table 3 shows the  $OP_m$  achieved by the ROI extraction algorithm for  
481 each muscle  $m$  in both experiments.

482 *5.2. Marbling prediction*

483 The texture features described in section 3.2 are computed for all the ham  
484 slices. In the experiment 1, the texture features are computed on the irregular

Muscle ( $m$ )	#images	$OP_m$	
		Experiment 3	Experiment 2
Biceps femoris	351	93.79	98.54
Semimembranosus	335	89.92	89.20
Semitendinosus	55	94.76	99.84

Table 3: Average percentage of overlapping pixels of the automatic extracted ROI (column **Experiment 3**) and the extraction from the centroid (column **Experiment 2**) with the true muscle annotated by the experts used in the experiment 1 for every muscle.

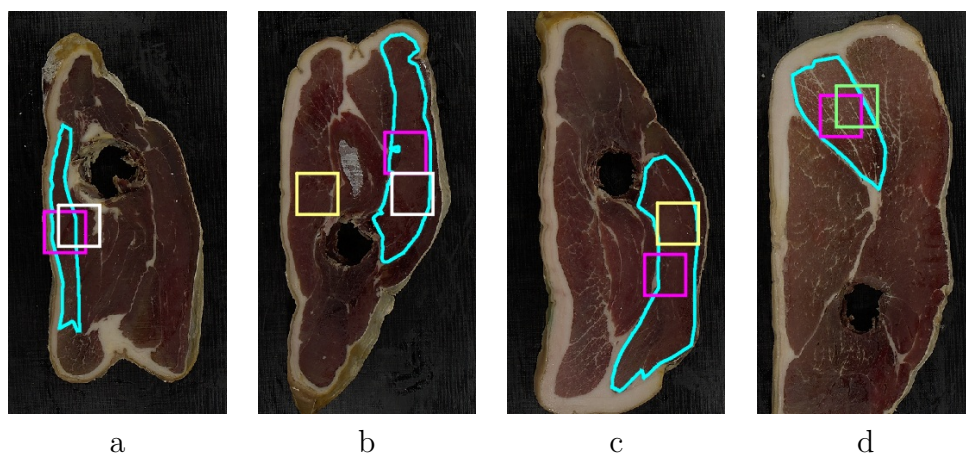


Figure 7: Examples of square ROI extraction, in cyan the muscle contour, in pink the square ROI extracted in the centroid, in white, yellow and green the square ROI automatically extracted for BF, SM and ST muscles respectively: a) ROI bigger than the BF muscle; b) the automatic ROI extractor fails in SM muscle; c) and d) suboptimal ROIs for SM and ST, respectively.

485 region,  $R_i$ , defined by each muscle and annotated by the food technology  
486 experts. So, Gabor and wavelet features were not computed because they  
487 must be applied on a square image. In experiment 2, squared regions  $RS_i$  of  
488 size  $64 \times 64$  pixels are extracted from the centroid of  $R_i$  and all the texture  
489 features were computed. In experiment 3, the texture features were computed  
490 on the square regions automatically extracted from the ham slice using the

491 algorithm described in the section 3.1.

Feature vector	Experiment 1		Experiment 2		Experiment 3	
	$R$	MAE	$R$	MAE	$R$	MAE
Pure color features						
CMRGB	0.85	0.62	0.79	0.70	0.72	0.79
CMab	0.69	0.82	0.63	0.86	0.58	0.93
CMVRGB	0.90	0.50	0.86	0.57	0.81	0.67
CMVab	0.74	0.75	0.66	0.83	0.68	0.86
FOSRGB	<b>0.91</b>	0.47	<b>0.87</b>	0.54	<b>0.84</b>	0.63
FOSab	0.81	0.68	0.74	0.76	0.71	0.78
Grey-level texture features						
HarRGB	<b>0.91</b>	0.49	<b>0.88</b>	0.56	<b>0.80</b>	0.72
HarLab	0.90	0.50	0.85	0.61	0.77	0.76
mlbpRGB	<b>0.93</b>	0.43	<b>0.83</b>	0.62	<b>0.73</b>	0.79
mlbpLab	0.92	0.45	0.81	0.66	0.71	0.80
WTrgbHaarLL	–	–	0.85	0.57	0.80	0.67
WTrgbHaarAll	–	–	0.88	0.54	0.80	0.66
WTLabHaarLL	–	–	0.85	0.57	0.80	0.67
WTLabHaarAll	–	–	<b>0.88</b>	0.54	<b>0.82</b>	0.65
WTrgbDb4LL	–	–	0.86	0.58	0.79	0.70
WTrgbDb4All	–	–	0.88	0.53	0.79	0.70
WTLabDb4LL	–	–	0.87	0.57	0.80	0.70
WTLabDb4All	–	–	0.89	0.53	0.79	0.70
GaborRGB	–	–	<b>0.89</b>	0.54	<b>0.80</b>	0.70
GaborLab	–	–	0.88	0.55	0.80	0.71
Color texture features						
CMVHarRGB	<b>0.95</b>	0.38	0.91	0.47	0.84	0.64
FOSHarRGB	0.95	0.39	<b>0.92</b>	0.46	0.83	0.63
CMVmlbpRGB	0.93	0.41	0.89	0.51	0.79	0.68
FOSmlbpRGB	0.94	0.40	0.90	0.48	0.80	0.67
CMVWTLabHaarAll	–	–	0.89	0.53	0.82	0.65
FOSWTLabHaarAll	–	–	0.89	0.51	0.83	0.62
CMVGaborRGB	–	–	0.91	0.48	0.82	0.65
FOSGaborRGB	–	–	0.91	0.48	0.82	0.64

Table 4: Correlation (column  $R$ ) and mean absolute error (column MAE) for the marbling prediction using pure color features (upper part of the table), grey level texture features (middle part of the table) and color texture features (lower part of the table) using the support vector regression (svr) for the three experiments.

492 Table 4 shows the correlation ( $R$ ) and the mean absolute error (MAE) for  
 493 marbling prediction using the support vector regression (svr) for the three

494 experiments. The feature vector FOSRGB achieved the highest  $R$  and lowest  
495 MAE among all pure color features (upper part of the table), with  $R=0.91$ ,  
496 0.87 and 0.84 in experiments 1, 2 and 3, respectively. As expected, when the  
497 performance of the automatic detection degrades, the regression accuracy  
498 decreases. But, it is still quite high for the third experiment, very good to  
499 excellent following the Colton’s criteria. In relation with grey-level texture  
500 features (middle part of table), the use of irregular regions of the muscle  
501 (experiment 1) achieves the highest performance ( $R=0.93$  and MAE=0.43  
502 using the texture vector mlbpRGB). In general, the performance achieved in  
503 experiment 2 is higher than the experiment 3 for all the features vectors used,  
504 noting the loss of information in the automatic selection of the ROIs. Com-  
505 paring the different families of grey-level texture features for square ROIs, the  
506 wavelet features achieve the highest performance for experiment 3 ( $R=0.82$   
507 and MAE=0.65) followed very close by the Haralick’s coefficients and Ga-  
508 bor features ( $R=0.80$ ), which means that the model is also from good to  
509 excellent. From the color space point of view, although the best results with  
510 wavelet features are achieved using the Lab color space, the difference with  
511 the use of RGB color space is not significant and the highest performance  
512 with the remaining feature vectors is better using RGB color space.

513 We developed experiments combining the best pure color features (vectors  
514 FOSRGB and CMVRGB) with the best grey-level texture features of each  
515 texture features families. Specifically, we chose the grey-level texture vectors  
516 HarRGB for Haralick’s coefficients, mlbpRGB for local binary patterns, WT-



517 LabHaarAll for wavelet features and GaborRGB for Gabor features. The  
518 results are shown in the lower part of table 4. The performance increases 0.2  
519 for the first experiment (from  $R=0.93$  for mlbpRGB to  $R=0.95$  for CMVHar-  
520 RGB) and 0.3 for the experiment 2 (from  $R=0.89$  for GaborRGB to  $R=0.92$   
521 for FosHarRGB), but  $R$  does not increase in experiment 3. In all the cases,  
522 the best results were achieved combining the color information (CMVRGB  
523 or FOSRGB vectors) and the grey-level texture information provided by the  
524 Haralick's or LBP coefficients (vector HarRGB and mlbpRGB). The MAE  
525 is a performance measure easier to interpret than  $R$  from the point of view  
526 of food technology experts. Figure 8 shows the reliability of the prediction  
527 using the **svr** regressor for experiments 1 (left panel) and **rf** regressor for  
528 experiment 3 (right panel) for the best feature vectors. The blue line rep-  
529 resents the true marbling for each ham slice provided by the experts. The  
530 red points represent the predicted marbling by **svr** or **rf** for each ham slice.  
531 The average difference between the blue and red values for each ham slice  
532 is the MAE (0.38 and 0.60 in the left and right panels, respectively). This  
533 means that the prediction of the computer is the true value  $\pm$  MAE in aver-  
534 age. Taking in mind that the expert's tolerance in the sensorial analysis to  
535 establish the marbling is 0.5, the prediction of the computer is comparable  
536 with the precision of the experts.

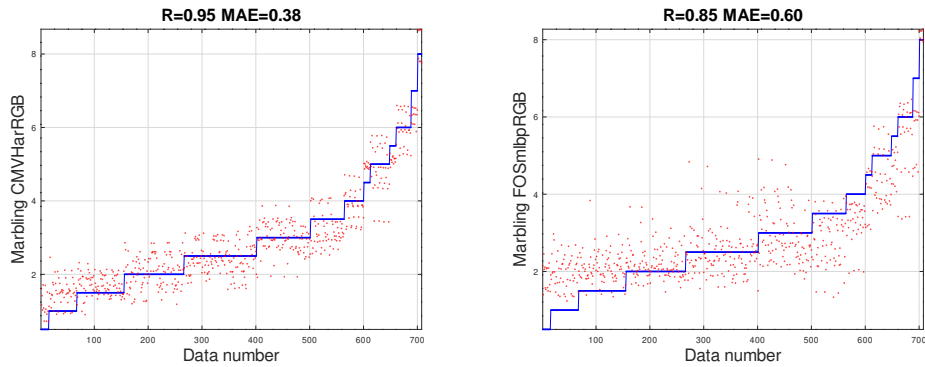


Figure 8: Graphical representation of the true (blue line) and predicted (red points) ham marbling (vertical axis) for all ham slices (horizontal axis) using the svr regressor: (left panel) using the CMVHarRGB vector in the experiment 1 and (right panel) using the FOSRGB plus LBPRGB vector in the experiment 3.

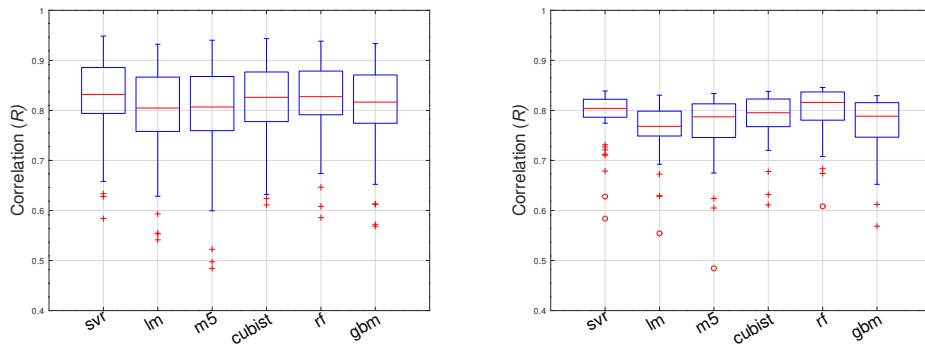


Figure 9: Box plots showing the correlation  $R$  for the different regressors (horizontal axis) considering all the experiments together (left panel) and only the experiment 3 (right panel).

537 *5.3. Comparing different regressors for marbling prediction*

538 In order to find the best prediction of marbling score, we applied the  
 539 regressors described in section 3.3 to the color texture features described in  
 540 section 3.2 for the three experiments. Figure 9 shows the box plots com-

541 paring the correlation for all regressors considering all feature vectors in the  
542 experiments 1, 2 and 3 (left panel) and only in experiment 3 (right panel).  
543 The upper and lower edges of each box indicate the 25th and 75th percentiles,  
544 respectively, the upper and lower blue segments enclose the remaining data  
545 and the red crosses are the data considered outliers. The red line inside the  
546 box is the median of the data. In both panels, there are not large difference  
547 among regressors. Considering the tree experiments (left panel), svr, rf and  
548 cubist have the highest medians, and svr has the smaller box, similar to rf  
549 but with higher median. In experiment 3 (right panel), the rf box shows the  
550 best median, followed by svr with a shorter box. Table 5 shows the color  
551 texture vector that achieved the highest correlation  $R$ , with the standard  
552 deviation over the  $K$  folds in the cross validation, for each regressor on the  
553 first (irregular regions for each muscle) and third experiments (square regions  
554 for each muscle). In experiment 3, the highest values of  $R$  are achieved by  
555 the rf regressor using the feature vector FOSmlbpRGB ( $R = 0.846 \pm 0.008$ ).  
556 Considering that the MAE values (0.38 and 0.60) reflect the dispersion of the  
557 computer marbling prediction from the true marbling values, the computer  
558 predictions fall near the experts' tolerance, which is 0.5. Hence, for the first  
559 experiment, the computer predicts correctly the 90.4% (67.8% for the third  
560 experiment) of samples within a tolerance of  $\pm 0.5$  (the expert's tolerance)  
561 and within a tolerance of  $\pm 1$ , the 99.3% (88.8% for the third experiment).

Regressor	Experiment 1		Experiment 3	
	Feature	$R$	Feature	$R$
lm	CMVmlbpRGB	$0.932 \pm 0.003$	FOSHArRGB	$0.831 \pm 0.014$
svr	CMVHarRGB	<b><math>0.948 \pm 0.004</math></b>	CMVHarRGB	<b><math>0.839 \pm 0.005</math></b>
m5	FOSmlbpRGB	$0.940 \pm 0.003$	FOSHArRGB	$0.834 \pm 0.017$
cubist	FOSmlbpRGB	$0.943 \pm 0.007$	FOSHArRGB	$0.838 \pm 0.012$
gbm	FOSmlbpRGB	$0.934 \pm 0.001$	FOSRGB	$0.829 \pm 0.013$
rf	FOSmlbpRGB	$0.938 \pm 0.004$	FOSmlbpRGB	<b><math>0.846 \pm 0.008</math></b>

Table 5: Correlation ( $R$ ) for the marbling prediction using all the regressors and the best feature vector (column Feature) for the first and third experiments.

562 *5.4. Comparing performance for different muscles*

563 In order to test if the regressor behaviour is stable over the different  
564 muscles, we create two datasets with images belonging to the third experi-  
565 ment: 1) BFData for images of *Biceps femoris* (BF) muscle; and 2) SMDData  
566 for images of *Semimembranosus* (SM) muscle. *Semitendinosus* muscle is not  
567 analysed because there are few images. For BF muscle, the best performance  
568 is achieved by the feature vector FOSGaborRGB using the `cubist` regres-  
569 sor ( $R=0.80$  and  $MAE=0.50$ ). For the SM muscle, the best performance is  
570 achieved by the feature vector FOSmlbpRGB using also the `cubist` regressor  
571 ( $R=0.74$  and  $MAE=0.55$ ). Although the correlation loss is 0.12 ( $0.92-0.80$ )  
572 and 0.18 ( $0.92-0.74$ ) for the BF and SM muscles respectively, the loss in  
573 MAE is only 0.04 ( $0.50-0.46$ ) and 0.09 ( $0.55-0.46$ ) respectively. Thus, the  
574 computer predictions with a tolerance of  $\pm 1$  are correct for the 93.5% of BF  
575 and 94.1% of SM muscles. This facts lead to conclude that our system is  
576 stable with the different muscles.

577 5.5. *Computation time*

578 In order to design a computer system to predict the marbling from a  
579 ham slice, which should operate in real time in the meat industry, it is very  
580 important the computational time needed by the different stages of the pro-  
581 cess. The experiments were performed on a desktop computer with Intel®  
582 Core™ i7-9700 processor at 3.6GHz and 64GB RAM memory under Ubuntu  
583 20.04. The algorithm for the extraction of a square ROIs for the different  
584 muscles was done in the C++ programming language using the computer vi-  
585 sion library OpenCV<sup>6</sup> and the remaining processing was done using Matlab  
586 2021a<sup>7</sup>. The average computational time to extract the ROIs was 18.7, 18.4  
587 and 19.9 miliseconds for *biceps*, *semimembranosus* and *semitendinosus* mus-  
588 cles, respectively. The time required to compute the color texture features  
589 depends on the method used and the type of experiment (irregular regions  
590 in experiment 1 and square regions in experiments 2 and 3). For square  
591 regions of  $64 \times 64$  pixels, the average computational time for each family of  
592 features was: 1) for pure color features the time ranges from 0.48 ms. for  
593 CMRGB to 2.21 ms. for FOSLab; 2) for Haralick's features: 7.59 and 9.20  
594 ms. for HarRGB and HarLab, respectively; 3) for LBP texture features,  
595 the time is 170.03 ms. for mlbpRGB and 172.20 ms. for mlbpLab; 4) for  
596 wavelet features (vectors  $WT_{ijk}$ , where  $i = \{Haar, Daub\}$ ,  $j = \{RGB, Lab\}$   
597 and  $k = \{LL, All\}$ ) the time ranges from 1.17 ms. for WTrgbHaarLL to 2.73

---

<sup>6</sup><https://opencv.org>

<sup>7</sup><https://mathworks.com>

598 ms for WTLabDb4All; and 5) for Gabor texture features: 19.17 and 20.99  
599 ms. for GaborRGB and GaborLab, respectively. The time spent by the  
600 svr regressor to predict the marbling using the texture feature vector is less  
601 than 1 milisecond per image. Overall, the computational time required by  
602 the whole process depicted in figure 4, discarding the acquisition of the ham  
603 slice image, can be estimated as 19 ms. for the automatic ROI extraction,  
604 plus less than 10 ms. for color texture feature computation, plus 1 ms. for  
605 regression model, summarized approximately 30 ms.

## 606 **6. Conclusions and future work**

607 This paper proposes a system to predict the marbling of dry-cured ham  
608 from a ham slice image. After the acquisition of ham image, a square ROI of  
609 the *semimembranosus* (SM), *semitendinosus* (ST) and *biceps femoris* (BF)  
610 muscles is automatically extracted using the procedure described by algo-  
611 rithm 1. The overlapping of the ROIs extracted by this method with the  
612 true muscle area is, in average, higher than 90% for all the muscles. The  
613 prediction of ham marbling using the support vector regression is: 1) a cor-  
614 relation  $R$  of 0.95 using the true ham muscles areas annotated by experts  
615 (experiment 1) and the feature vector CMVHarRGB, composed by the mean  
616 and variance of each channel of RGB color image combined with the Har-  
617 alick's coefficients of the grey-level image; and 2)  $R=0.85$  for square ROIs  
618 automatically extracted, in the experiment 3, using the feature vector FOS-  
619 mlpbRGB (statistics of each channel of RGB color image combined with the

620 MLBP texture features of the grey-level image). The MAE achieved is 0.38  
621 in the first case and 0.60 in the second one. These values are comparable to  
622 0.5, which is the estimated standard deviation of the panelists. This leads  
623 to think that the computer system can perform the prediction similarly to  
624 a human expert. The computational time to do the prediction (without the  
625 image acquisition time) is approximately 30 milliseconds to extract the square  
626 ROI, compute the color texture features and predict the marbling in a general  
627 purpose personal computer.

628 The good results and high speed of the marbling prediction for sliced dry-  
629 cured ham suggest that this application could be deployed in the dry-cured  
630 ham industry. Future work will be the development of a software to predict  
631 the marbling and other dry-cured sensorial measures.

## 632 **Acknowledgments**

633 This work has received financial support from the Xunta de Galicia (Cen-  
634 tro singular de investigación de Galicia, accreditation 2020–2023) and the  
635 European Union (European Regional Development Fund—ERDF), Project  
636 ED431G-2019/04. IRTA’s contribution was also funded by the CCLabel  
637 project (RTI-2018- 096883-R-C41) and the CERCA programme from Gen-  
638 eralitat de Catalunya.

639 **References**

- 640 E. Coll-Brasas, P. Gou, J. Arnau, A. Olmos, E. Fulladosa, Processing param-  
641 eters involved in the development of texture and tyrosine precipitates in  
642 dry-cured ham: Modelisation of texture development, *Meat Sci* 172 (2021)  
643 108362. doi:<https://doi.org/10.1016/j.meatsci.2020.108362>.
- 644 L. Lorido, E. Pizarro, M. Estévez, S. Ventanas, Emotional re-  
645 sponses to the consumption of dry-cured hams by spanish con-  
646 sumers: A temporal approach, *Meat Sci* 149 (2019) 126–133.  
647 doi:<https://doi.org/10.1016/j.meatsci.2018.11.015>.
- 648 M. de Prados, E. Fulladosa, P. Gou, I. Muñoz, J. Garcia-Perez,  
649 J. Benedito, Non-destructive determination of fat content in green  
650 hams using ultrasound and x-rays, *Meat Sci* 104 (2015) 37–43.  
651 doi:<https://doi.org/10.1016/j.meatsci.2015.01.015>.
- 652 E. Cernadas, M. Durán, T. Antequera, Recognizing marbling in dry-cured  
653 Iberian ham by multiscale analysis, *Patt Recog Lett* 23 (2002) 1311–1321.
- 654 D. Moines, *Marbling standards*, National Pork Producers Council, 1999.
- 655 M. K. Dutta, A. Issac, N. Minhas, B. Sarkar, Image processing based method  
656 to assess fish quality and freshness, *J Food Engin* 177 (2016) 50–58.  
657 doi:<https://doi.org/10.1016/j.jfoodeng.2015.12.018>.
- 658 J. Dias, P. Lage, A. Garrido, E. Machado, C. Conceição, S. Gomes, A. Mar-  
659 tins, A. Paulino, M. Duarte, N. Alvarenga, Evaluation of gas holes in



- 660 "Queijo de Nisa" PDO cheese using computer vision, *J Food Sci Technol* 58  
661 (2021) 1072–1080. doi:<https://doi.org/10.1007/s13197-020-04621-0>.
- 662 S. Srivastava, S. Vaddadi, S. Sadistap, Quality assessment of commercial  
663 bread samples based on breadcrumb features and freshness analysis using  
664 an ultrasonic machine vision (uvs) system, *J Food Meas Charact* 9 (2015)  
665 525–540.
- 666 E. Cernadas, P. Carrión, P. G. Rodríguez, E. Muriel, T. Antequera, Analyz-  
667 ing magnetic resonance images of Iberian pork loin to predict its sensorial  
668 characteristics, *Comput. Vis. Image Und.* 98 (2005) 345–361.
- 669 M. Ávila, M. Durán, T. Antequera, D. Caballero, T. Palacios-Pérez, E. Cer-  
670 nadas, M. Fernández-Delgado, Magnetic resonance imaging, texture anal-  
671 ysis and regression techniques to non-destructively predict the quality  
672 characteristics of meat pieces, *Engin Appl Artif Intel* 82 (2019) 110–125.  
673 doi:[10.1016/j.engappai.2019.03.026](https://doi.org/10.1016/j.engappai.2019.03.026).
- 674 P. Jackman, D.-W. Sun, P. Allen, Automatic segmenta-  
675 tion of beef longissimus dorsi muscle and marbling by  
676 an adaptable algorithm, *Meat Sci* 83 (2009) 187–194.  
677 doi:<https://doi.org/10.1016/j.meatsci.2009.03.010>.
- 678 J.-H. Liu, X. Sun, J. Young, L. Bachmeier, D. Newman, Predicting pork  
679 loin intramuscular fat using computer vision system, *Meat Sci* 143 (2018)  
680 18–23. doi:<https://doi.org/10.1016/j.meatsci.2018.03.020>.

- 681 B. Uttaro, S. Zawadski, I. Larsen, M. Juárez, An image  
682 analysis approach to identification and measurement of mar-  
683 bling in the intact pork loin, *Meat Sci* 179 (2021) 108549.  
684 doi:<https://doi.org/10.1016/j.meatsci.2021.108549>.
- 685 E. Santos-Garcés, I. Muñoz, P. Gou, N. Garcia-Gil, E. Ful-  
686 ladosa, Including estimated intramuscular fat content from  
687 computed tomography images improves prediction accuracy of  
688 dry-cured ham composition, *Meat Sci* 96 (2014) 943–947.  
689 doi:<https://doi.org/10.1016/j.meatsci.2013.09.018>.
- 690 I. Muñoz, P. Gou, E. Fulladosa, Computer image analysis for intramuscu-  
691 lar fat segmentation in dry-cured ham slices using convolutional neural  
692 networks, *Food Control* 106 (2019) 10.
- 693 L. Faucitano, J. Rivest, J. P. Daigle, J. Lévesque, C. Gariépy, Distribu-  
694 tion of intramuscular fat content and marbling within the longissimus  
695 muscle of pigs, *Canadian Journal of Animal Science* 84 (2004) 57–61.  
696 doi:10.4141/A03-064.
- 697 L. Liu, M. Ngadi, S. Prasher, C. Gariépy, Objective determination of pork  
698 marbling scores using the wide line detector, *J Food Engin* 110 (2012)  
699 497–504. doi:<https://doi.org/10.1016/j.jfoodeng.2011.11.008>.
- 700 H. Huang, L. Liu, M. Ngadi, C. Gariépy, Prediction of pork marbling

701 scores using pattern analysis techniques, *Food Control* 31 (2013) 224–229.  
702 doi:<https://doi.org/10.1016/j.foodcont.2012.09.034>.

703 I. Muñoz, M. Rubio-Celorio, N. Garcia-Gil, M. D. Guàrdia, E. Fulla-  
704 dosa, Computer image analysis as a tool for classifying marbling:  
705 A case study in dry-cured ham, *J Food Engin* 166 (2015) 148–155.  
706 doi:<https://doi.org/10.1016/j.jfoodeng.2015.06.004>.

707 L. Velásquez, J. Cruz-Tirado, R. Siche, R. Quevedo, An ap-  
708 plication based on the decision tree to classify the marbling of  
709 beef by hyperspectral imaging, *Meat Sci* 133 (2017) 43–50.  
710 doi:<https://doi.org/10.1016/j.meatsci.2017.06.002>.

711 R. Bermúdez, D. Franco, J. Carballo, J. Lorenzo, Physicochemical changes  
712 during manufacture and final sensory characteristics of dry-cured Celta  
713 ham. Effect of muscle type, *Food Control* 43 (2014) 263–269.

714 E. Cernadas, M. Fernández-Delgado, E. González-Rufino, P. Carrión, In-  
715 fluence of normalization and color space to color texture classification,  
716 *Pattern Recogn.* 61 (2017) 120 – 138.

717 N. Otsu, A threshold selection method from gray-level histograms, *IEEE*  
718 *Trans Syst Man Cyb* 9 (1979) 62–66. doi:10.1109/TSMC.1979.4310076.

719 E. González-Rufino, P. Carrión, E. Cernadas, M. Fernández-Delgado,  
720 R. Domínguez-Petit, Exhaustive comparison of colour texture features

721 and classification methods to discriminate cells categories in histological  
722 images of fish ovary, *Pattern Recogn.* 46 (2013) 2391–2407.

723 R. M. Haralick, K. Shanmugan, I. Dinstein, Textural features for image  
724 classification, *IEEE T Man Cyb.* 3 (6) (1973) 610 – 621.

725 T. Ojala, M. Piaticäinen, T. Mäenpää, Multiresolution grey-scale and rota-  
726 tion invariant texture classification with Local Binary Pattern, *IEEE T*  
727 *Pattern Anal.* 24 (7) (2002) 971–987.

728 J. S. Walker, *A Primer on wavelets and Their Scientific Applications*, Chap-  
729 man Hall, 2008.

730 A. Laine, J. Fan, Texture classification by Wavelet Packet signatures, *IEEE*  
731 *T Pattern Anal.* 15 (11) (1993) 1186–1191.

732 T. Randen, J. H. Husoy, Filtering for Texture Classification: A Comparative  
733 Study, *IEEE T Pattern Anal.* 21 (4) (1999) 291–310.

734 F. Bianconi, A. Fernández, Evaluation of the effects of Gabor filter paramete-  
735 rs on texture classification, *Pattern Recogn.* 40 (2007) 3325–3335.

736 M. Fernández-Delgado, M. Sirsat, E. Cernadas, S. Alawadi, S. Barro,  
737 M. Febrero-Bande, An extensive experimental survey of regression meth-  
738 ods, *Neural Netw* 111 (2019) 11–34. doi:10.1016/j.neunet.2018.12.010.

739 M. Kuhn, *Caret: Classification and regression training*, 2016. R package  
740 version 6.0-70.

- 741 D. Bates, J. Chambers, Statistical models in S, Wadsworth & Brooks/Cole,  
742 Pacific Grove, CA, 1992.
- 743 C. Chang, C. Lin, LIBSVM: a library for support vector machines, ACM T  
744 Intel. Syst. Tec. 2 (2011) 27:1–27:27.
- 745 R. Quinlan, Learning with continuous classes, in: Proc. Australian J. Conf.  
746 on Artif. Intel., 1992, pp. 343–348.
- 747 R. Quinlan, Combining instance-based and model-based learning, in: Proc.  
748 Intl. Conf. on Mach. Learn., 1993, pp. 236–243.
- 749 L. Breiman, Random forests, Mach Learn 45 (2001) 5–32.
- 750 T. Colton, Statistical in medicine, Little Brown and Co., NJ, 1974.